Performance Evaluation of the SmartBrain: A Wearable PET System for Human Brain Imaging

Han Liu[1,2], Wenkang Qu[1], Da Liang[1], Xin Yu[1], Yuejie Lin[1], Haoyu Zhou[1], Siyuan Han[1], Zhijun Zhao[1], Ying Lin[1], Xiaoyin Zhang[1], Jinyong Tao[1], Wenbin Li[1], Huiping Zhao[1], Yibin Zhang[1], Gongning Luo[2] , Ningyi Jiang[3], Qiyu Peng[1]*
[1]Institute of Biomedical Engineering, Shenzhen Bay Laboratory, Shenzhen, China
[2]College of Artificial Intelligence, Harbin Institute of Technology, Harbin, China
[3]Department of Nuclear Medicine, The Seventh Affiliated Hospital, Sun Yat-sen University, Shenzhen, China

Abstract—Background. Positron Emission Tomography (PET) is a vital medical imaging tool for studying in vivo metabolism. However, conventional PET systems are limited in their inability to image during free movement. Therefore, we have developed a wearable brain PET system for real-time imaging, called SmartBrain. ***Methods.*** The SmartBrain used 192 detectors and the detector consists of a 6 × 6 lutetium-yttrium oxyorthosilicate crystal (3 × 3 × 5 mm^3) array with 3 × 3 silicon photomultipliers array. We evaluated the physical performance of SmartBrain according to the National Electrical Manufacturers Association (NEMA) NU 2-2018 standard. In addition, we performed ^{18}F-FDG imaging using a custom Hoffman brain phantom and a multi-layer Derenzo phantom. Dynamic rat images and the ^{18}F-FDG images from a healthy volunteer are presented. ***Results.*** Spatial resolution is 2.29 mm in center of field of view (FOV). The sensitivity was 720.15 cps/MBq. The peak noise-equivalent count rate was 4.67 kcps at 10.11 kBq/ml, and the scatter fraction was 29.53%. The NEMA image-quality contrast recovery coefficients varied from 72.85% (10-mm sphere) to 89.40% (37-mm sphere), and background variability was 11.25% at a contrast of 9.36:1. The time-of-flight (TOF) resolution was 234.22 ps, and the energy resolution was 10.81%. The SmartBrain showed that the main structures of Hoffman brain phantom could be resolved and demonstrated the ability to separate rods as small as 1.7 mm. In addition, an example of the structure of the human brain was demonstrated. ***Conclusion.*** The SmartBrain clearly demonstrated brain structures, confirming its suitability for clinical brain research. Moreover, as a wearable and mobile PET platform, it offers unique opportunities for naturalistic brain imaging and future clinical applications in the diagnosis and management of neurological disorders.

Keywords— Wearable PET, Human brain imaging, NEMA, SmartBrain

I. Introduction

Human brain research is essential for understanding cognition, emotion, and behavior. Brain PET is a powerful imaging modality that directly reflects cerebral metabolic activity, making it an essential tool for human brain research (1,2). However, conventional brain PET typically requires subjects to remain stationary in a sitting or supine position during scanning, which poses limitations for certain patient populations, such as children, individuals with epilepsy, or patients with other neurological disorders. Wearable brain PET systems aim to address these challenges by enabling brain metabolism studies in more natural or even dynamic conditions, thereby expanding the potential applications of brain PET in neuroscience and clinical research. Moreover, wearable brain PET systems are highly portable, require less space, and are more cost-effective, which could allow this technology to be extended to a broader user base, benefiting more people.

Despite this potential, research on mobile or wearable brain PET systems remains at an early stage. In 2011, Yamamoto and colleagues from Nagoya University, Japan, developed a seated PET brain imaging system specifically designed for human studies, known as PET-Hat (3). Subsequently, Tashima's team in Japan introduced a similar seated PET system known as Helmet-Chin PET (4). However, both systems require stationary mounting platforms, limiting their use in portable imaging contexts. In 2017, Brefczynski-Lewis's group at West Virginia University developed a semi-mobile brain PET system, known as AM-PET (5), by mounting the PET scanner on an externally movable support. In the same year, Peng's group further advanced this technology by creating the Mind-tracker PET (6), a fully wearable brain PET system weighing only 3.5 kg that operated without an external support structure. However, both AM-PET and Mind-tracker PET had limited axial fields of view (50 mm and 30 mm, respectively), restricting imaging to small regions of the brain. Moreover, these systems lacked TOF measurement capabilities (7).

This work aims to develop a wearable brain PET system capable of imaging in free movement. To verify whether the SmartBrain PET can meet the basic standards of commercial PETs, we have evaluated system performance using the NEMA NU 2-2018 standards and compare it with the GE Discovery MI PET/CT system (GE DMI) to ensure its practicality and effectiveness. And we will validate its potential value in real-world scenarios in future work.

II. METHODS

A. System Parameters

The SmartBrain PET system features a 16-sided polygonal ring with an inner diameter of 207.44 mm and an axial field of view (AFOV) of 121 mm, covering the entire brain (Figure 1). It consists of 192 detector modules arranged in six rings, with 32 modules per ring with 0.5 mm axial and tangential gaps. Each module comprises a 6 × 6 array of $3 \times 3 \times 5\ \text{mm}^3$ lutetium-yttrium oxyorthosilicate (LYSO) crystals, optically coupled via optical adhesive to a 3 × 3 array of 6-mm silicon photomultipliers (SiPMs; onsemi, Phoenix, AZ, USA).

A channel reduction strategy decreases the total number of readout channels from 1,728 to 432. Each detector module integrates a 3 × 3 SiPM array. Four modules are combined in a 2 × 2 configuration, and signals are hierarchically multiplexed from 36 channels to 9 by encoding three rows, three columns, and three logical layers, with the fourth layer inferred from the others (8). To further reduce system weight, the 5-mm-thick crystals were used, at the cost of lower sensitivity and signal-to-noise ratio (SNR). Future integration of TOF is expected to improve SNR (9). The use of channel reduction and lightweight crystals results in an overall system weight of approximately 6 kg.

The system supports list-mode acquisition (461–611 keV energy window, 1 ns coincidence window), with a decoding algorithm ensuring accurate event positioning. Data are timestamped for flexible post-processing, supporting TOF and dynamic imaging. Two mechanical support systems were developed: a wearable backpack and a suspension system (Figure 1). Temperature is stabilized within 0.5 ℃ using external fans and air-cooled ducts.

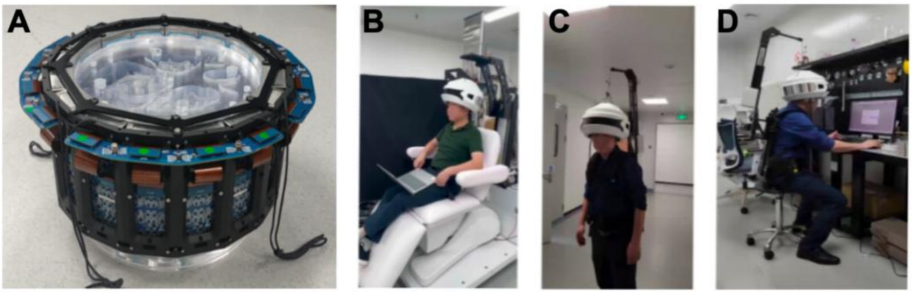

FIGURE 1. The SmartBrain PET system. (A) System composed of detectors and SiPMs with Hoffman phantom. (B) Seated-position scanning. (C) Backpack system permitting data collection in ambulatory states. (D) Workstation scenario demonstrating natural seated use.

B. NEMA NU 2-2018 Performance evaluation

Physical performance was evaluated according to the NEMA NU 2-2018 standards (10), including spatial resolution, sensitivity, count rate performance, accuracy of corrections, image quality, energy and timing resolution.

Spatial Resolution. Spatial resolution was measured at 16 different locations, with 60-second acquisitions at each point (8 points at the center of the axial FOV, 8 points at one-eighth of the axial FOV from the end of the tomography), using a 0.25 mm ^{22}Na point source (0.444 MBq) embedded in a solid disk. The data were reconstructed using a two-dimensional filtered backprojection (FBP2D) algorithm without any correction, with a voxel size of 0.543 × 0.543 × 1.625 mm^3. To meet the NEMA requirement that the voxel size be smaller than one-third of the full width at half maximum (FWHM), the reconstructed images were resampled using trilinear interpolation to achieve an isotropic voxel size of 0.5 × 0.5 × 0.5 mm^3. Axial, radial, and tangential resolutions were evaluated according to the NEMA NU 2-2018 standard.

Sensitivity. Sensitivity measurements were performed using a NEMA PET sensitivity phantom consisting of five concentric aluminum sleeves, each 70 cm in length. A 70-cm polyethylene tube filled with 5.1 MBq of ^{18}F-FDG solution was inserted into the aluminum sleeves, positioned both at the center of the transaxial FOV and 5 cm off-center. Ten 600-second acquisitions were conducted, successively removing the outermost sleeve to estimate attenuation-free sensitivity. The collected list-mode data were binned into sinograms using single-slice rebinning to estimate both total sensitivity and axial slice sensitivity.

Count Rate Performance. Count rate performance was evaluated using a scatter phantom consisting of a 14 cm long polyethylene cylinder with a 10 cm diameter. The line source was initially loaded with 41.86 MBq of ^{18}F-FDG at the first measurement start and 1.17 MBq at the last measurement start. In total, we scanned 34 frames with 60 s durations as the activity decayed. System count rates were plotted alongside activity concentrations, including trues, randoms, scatters, total counts, the noise-equivalent count rate and scatter fraction without any correction.

Image Quality. We developed a brain-sized image quality phantom to replace the human torso, which had six spheres as the original phantom. A cylindrical phantom with a liquid-filled diameter of 19 cm was filled with ^{18}F-FDG at a background activity concentration of 4.06 kBq/ml. Six spheres with diameters of 10, 13, 17, 22, 28 and 37 mm were filled with the ^{18}F-FDG solution at an activity concentration with a sphere-to-background ratio of 9.36:1. Measurement duration was 60 min. Contrast of hot spheres (QH) and background variability (Nj) were measured. To evaluate background variability, twelve circular ROIs were placed on the background uniform region over 5 axial slices (60 ROIs in total), with the same diameter as hot sphere. Images were reconstructed using the ordered-subset expectation maximization (OSEM) algorithm for 12 iterations with 4 subsets. Only point spread function (PSF) modeling (2-mm Gaussian kernel) and attenuation correction were applied. The voxel size was 1 × 1 × 1 mm^3 and the shape matrix size was 217 × 217 × 120.

Engergy and Timing Resolution. Energy and timing resolution were assessed using a scaled-down NEMA scatter fraction phantom with ~10.55 MBq of ^{18}F-FDG. The central axis of the phantom coincided with the PET z-axis, and the radioactive source was positioned based on the TOF-free OSEM reconstructed image. According to the NEMA standard, LORs more than 20 mm from the radioactive source were discarded, and scattering and random events were estimated and subtracted from the tail of the histogram (time bin = 10 ps). We used a six-line source positioned 50 mm from the center to perform system timing calibration. Each line source had an inner diameter of 0.8 mm and a length of 140 mm, with an injected activity of 10.17 MBq for ^{18}F-FDG. Data were acquired for 20 min with an energy window from 461 to 611 keV and the initial coincidence timing window of ± 5 ns.

Timing calibration was iteratively performed after LOR selection until the change in timing resolution between iterations was less than 1 ps, after which a narrower timing window was applied (11).

C. Phantom Studies

The Multi-layer-Derenzo phantom used in this study was filled with an initial activity of 14.45 MBq of ^{18}F-FDG and scanned for 70 minutes for imaging evaluations. The phantom (Supplemental Figure1) consists of three layers of rod sources with varing diameters: top layer (1.5, 1.6, 1.7, 1.8, 1.9 and 2.0 mm; rod height: 35.5 mm), middle layer (2.0, 2.4, 2.8, 3.2, 3.6 and 4.0 mm; rod height: 20.0 mm) and bottom layer (2.5, 3.0, 3.5, 4.0, 4.5 and 5.0 mm; rod height: 80.0 mm). The rods were arranged in a standard hexagonal pattern, allowing resolution comparisons across a range of feature sizes in a single acquisition. The phantom was positioned at the center of the FOV with a 5-mm offset. Images were reconstructed using the OSEM algorithm (12 iterations, 4 subsets) with PSF modeling (2-mm Gaussian kernel), with and without TOF information. The voxel size was $0.5 \times 0.5 \times 0.5$ mm^3 and the shape matrix size was 217 × 217 × 217. Three experiments were performed; one TOF-enabled central placement is shown in the main text, and the other two (non-TOF, central and 5-cm off-center) are presented in the Supplemental Material.

Additionally, a custom-designed Hoffman brain phantom was prepared and filled with 24.01 MBq of ^{18}F-FDG, followed by 15-minute scan. The phantom had an outer diameter of 210 mm, a thickness of 146 mm, a liquid-filled diameter of 190 mm, and an axial extent of 95 mm. The brain-structure insert consisted of 19 slices, each 5 mm thick, with a maximum diameter of 148.24 mm and the same axial length of 95 mm (Supplemental Figure 2). In this design, the gray matter regions contained radioactivity, whereas the white matter and ventricular regions were non-radioactive. Images were reconstructed using the OSEM algorithm (12 iterations, 4 subsets) with random, attenuation, scatter correction, as well as PSF modeling (3-mm Gaussian kernel) incorporating TOF information. Since the system is not equipped with CT, attenuation correction was performed using a uniform cylindrical attenuation map with the same size as the phantom. The voxel size was $1 \times 1 \times 1$ mm^3 and the shape matrix size was 217 × 217 × 120.

D. Human Study

A 43-y-old male patient with epilepsy participated in a brain ^{18}F-FDG PET protocol approved by the Medical Ethics Committee of the Seventh Affiliated Hospital of Sun Yat-sen University. The blood glucose level was 100.8 mg/dl, and the injected activity was 318.2 MBq.

A comparative evaluation was performed between the SmartBrain PET system and the GE DMI PET/CT scanner. First, an 8-minute PET/CT scan was acquired on the GE DMI at ~60 minutes post-injection, with the subject at rest. Images were reconstructed using OSEM (2 iterations, 17 subsets) with TOF and standard corrections (attenuation, scatter, randoms, normalization, calibration, dead time). The voxel size was 1.30208 × 1.30208 × 2.79 mm^3 and the shape matrix size was 384 × 384 × 71.

Subsequently, a 60-minute PET scan on the SmartBrain PET system was performed at 190 minutes' post-injection (activity ~95.87 MBq). Images were reconstructed using OSEM (12 iterations, 4 subsets) with random, attenuation, and scatter corrections, as well as PSF modeling (3-mm Gaussian kernel) incorporating TOF information. The reconstructed images contained 217 × 217 × 120 voxels with a voxel size of 1 × 1 × 1 mm^3. CT images from the GE DMI PET/CT were used for attenuation correction.

III. RESULTS

A. The results of NEMA NU 2-2018 Performance Evaluation

The averaged FBP2D spatial resolution at the center of the axial FOV was 2.29 mm, as shown in TABLE 1. The apparent Gibbs phenomenon observed at off-center positions is more likely due to limited angular sampling and crystal width. By adding background noise and performing 1000 iterations of the reconstruction algorithm (12), the spatial resolution converged to 1.7 mm (Supplemental Figure 3 and Supplemental Figure 4), which is consistent with the Derenzo phantom results (Supplemental Figure 5). The total system sensitivity was 720.15 cps/MBq at the center in 461-611 keV in Figure 2 (B). The measured average system TOF resolution was 234.22 ps in Figure 2 (C), and the energy resolution was 10.81% (at FWHM). The peak noise-equivalent count rate was 4.67 kcps at an activity concentration of 10.11 kBq/mL in Figure 2 (D), and scatter fraction was 29.53%. The NEMA image-quality contrast recovery coefficients varied from 72.85% (10-mm sphere) to 89.40%, and the background variability (BV) varied was 11.25% (12 iterations and 4 subsets) in TABLE 2.

B. The results of Phantom Studies

Figure 3 shows multi-layer Derenzo phantom at the center of the FOV with TOF-OSEM, where the 1.7-mm hot rods were clearly separated. Supplemental Figure 5 further demonstrates that all 1.7-mm rods exhibited valley-to-peak ratios below 0.735, confirming effective separation. In addition, Supplemental Figure 6 illustrates that even without TOF reconstruction, the 1.7-mm rods remained resolvable both at the central and 5-cm off-center positions, indicating robust spatial resolution across the FOV.

Figure 4 shows reconstructed images of the Hoffman brain phantom. Transaxial, coronal, and sagittal slices demonstrate clear visualization of cortical gray matter activity, with distinct separation from non-radioactive white matter and ventricular regions. The images reproduce the complex gyral patterns of the cortex, highlighting the system's ability to resolve detailed brain anatomy. These findings complement the Derenzo phantom results, confirming both fine spatial resolution and realistic brain-structure imaging capability.

C. The results of Human Study

Figure 5 shows reconstructed human brain images acquired with the SmartBrain PET system. Transaxial, coronal, and sagittal views clearly depict cortical uptake patterns, with well-defined gray matter distribution and preserved gyral anatomy. The white matter and ventricular regions exhibited low-to-no activity, consistent with the expected ^{18}F-FDG distribution. These images confirm that the SmartBrain system can reliably capture fine structural details of the human brain, even in prolonged acquisitions.

Figure 6 compares brain images acquired with the SmartBrain PET system and the GE DMI PET/CT scanner. The GE DMI PET/CT images (top row) demonstrate high image quality under conventional whole-body PET/CT conditions. The SmartBrain images (bottom row) similarly reveal detailed cortical uptake patterns, with distinct gyral structures. Notably, the SmartBrain PET demonstrated enhanced visualization of cortical features (red arrows) despite the later imaging time point (~190 min post-injection, with reduced activity). This comparison highlights the SmartBrain system's high spatial resolution, supporting its suitability for brain-focused clinical research.

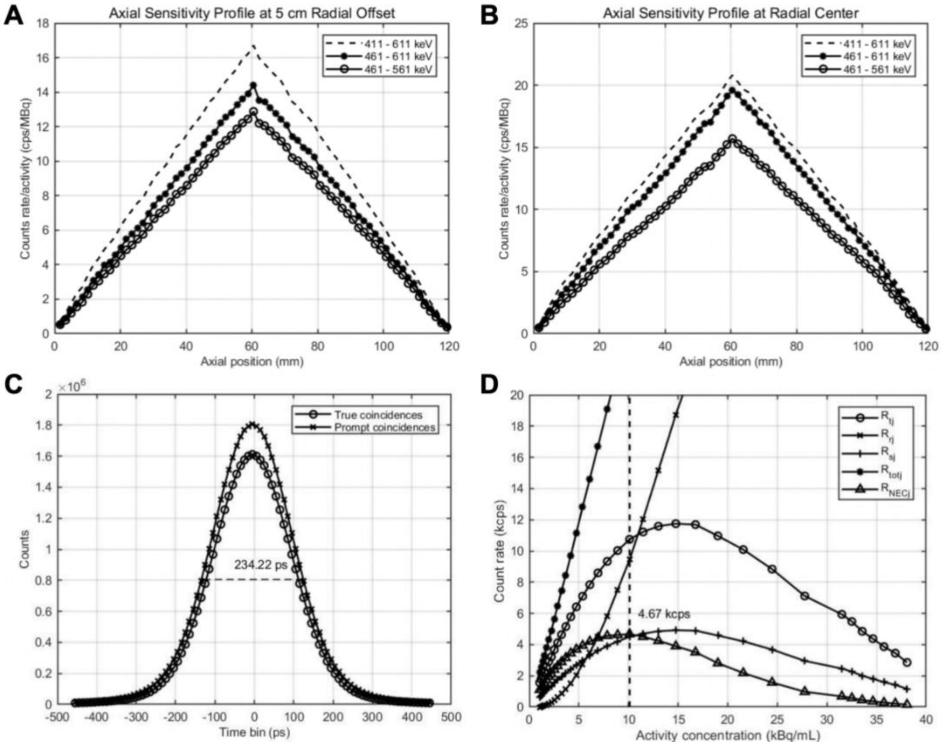

FIGURE 2. (A) Axial sensitivity profile with the line source at 5-cm radial offset. (B) Axial sensitivity profile with the line source at the center of the FOV. (C) TOF resolution with 20 ps time bins. (D) Trues, randoms, scatters, prompts, and noise-equivalent count rate.

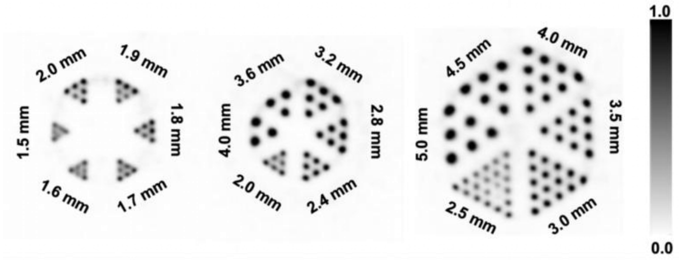

FIGURE 3. Multi-layer-Derenzo phantom imaging. Reconstructed images demonstrate hot-rod groups with diameters ranging from 1.5 to 5.0 mm.

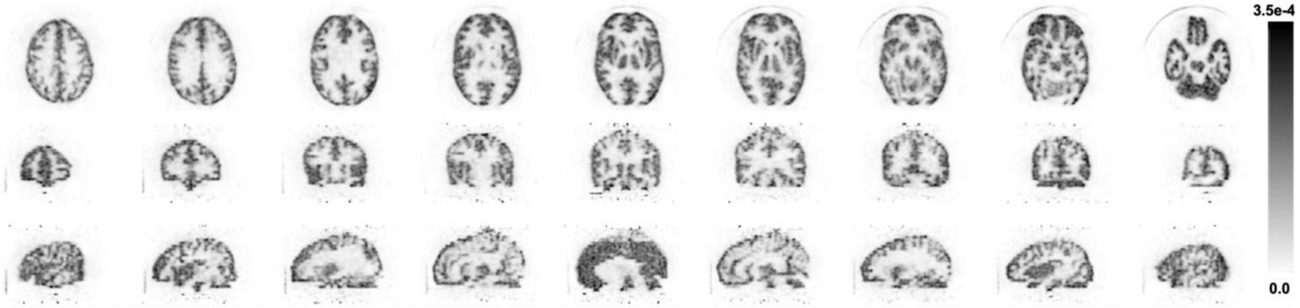

FIGURE 4. Hoffman brain phantom imaging results. Representative transaxial (top row), coronal (middle row), and sagittal (bottom row) slices reconstructed with TOF-OSEM. The gray matter shows distinct uptake, while white matter and ventricular regions exhibit no activity, allowing cortical structures and gyral patterns to be clearly visualized.

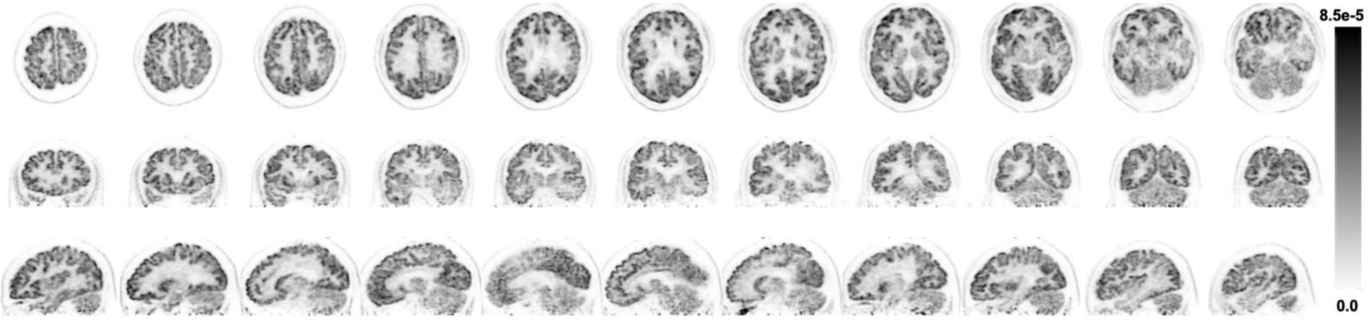

FIGURE 5. Human brain ^{18}F-FDG images acquired with the SmartBrain PET system. Transaxial (top), coronal (middle), and sagittal (bottom) views show clear cortical uptake and preserved gyral structures.

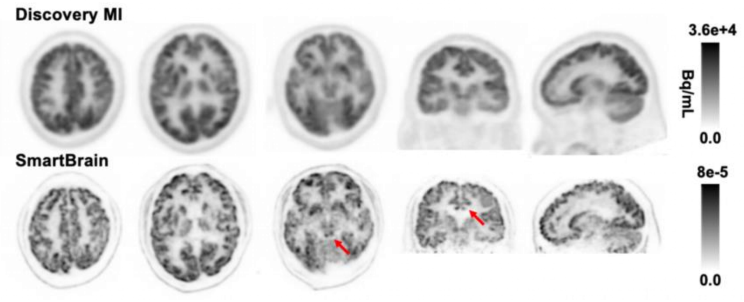

FIGURE 6. Comparison of human brain ^{18}F-FDG images between the GE DMI PET/CT (top row) and the SmartBrain PET system (bottom row). Both systems reveal cortical uptake patterns, while SmartBrain provides enhanced delineation of gyral details (red arrows). DMI images are displayed in calibrated units (Bq/mL). SmartBrain images were not cross-calibrated; the reconstructed voxel values are proportional to activity concentration but expressed in relative units.

IV. DISCUSSION

The SmartBrain PET system represents one of the few truly wearable brain PET systems capable of imaging under free-moving conditions. It demonstrated excellent spatial resolution, with point-source measurements at the center yielding 2.29 mm and clear resolution of 1.7 mm rods in the multi-layer Derenzo phantom, meeting the requirements for human brain imaging. In human studies, although the sensitivity of the wearable system is lower than the GE DMI PET/CT system (13), a 60-minute scan acquired after low-dose ^{18}F-FDG injection provided clear delineation of brain structures (Figure 5), with good comfort and feasibility during wear. Furthermore, after applying delay calibration algorithms, the system achieved a timing resolution of 234.22 ps. These results highlight the potential for future human imaging with higher tolerated activity and reduced scan times.

Several design features contribute to SmartBrain's performance. First, its full-ring configuration ensures complete FOV coverage with spatial resolution maintained across both central and off-center regions. Second, the use of short 5-mm crystals minimizes DOI uncertainty and reduces Compton scatter within the crystal. Third, the 3-mm crystal pitch further limits inter-crystal scatter and supports high-resolution imaging. Fourth, the compact bore size (20 cm) decreases the impact of non-collinearity, which is particularly advantageous in brain imaging. Finally, the incorporation of TOF (14, 15) reconstruction significantly improves image quality and compensates for reduced sensitivity relative to large clinical PET/CT systems. Together, these elements explain why SmartBrain achieves high spatial resolution and clear visualization of brain structures despite its compact and lightweight design.

Compared to conventional brain PET systems (16, 17), SmartBrain offers unique advantages in mobility, cost, and user comfort. Systems (18, 19) such as Vrain (20) and NeuroExplorer (21) achieve high sensitivity and image quality but remain large and stationary. In contrast, SmartBrain's compact detector design, lightweight electronics, and optimized mechanical structure significantly reduce system weight and cost, enabling wearable use. Compared with previous wearable PET prototypes such as AM-PET (22) and MindTracker, SmartBrain shows improvements in spatial resolution and axial coverage, and supports dynamic imaging under naturalistic conditions. Design elements such as flexible padding and ergonomic support help minimize motion-related artifacts during wear.

Nonetheless, current limitations remain. The system's thinner crystals result in lower sensitivity, and while TOF has been implemented, further improvements in detector coverage and sensitivity are needed. In addition, the absence of pile-up correction constrains performance under higher count-rate conditions, and fast dynamic studies remain challenging. Future optimization—including enhanced detector geometry, advanced correction algorithms, and AI-assisted image reconstruction (23, 24, 25) will further improve image quality, reduce acquisition times, and expand the scope of clinical and neuroscientific applications.

V. CONCLUSION

In this study, we developed and validated the SmartBrain wearable brain PET system, which demonstrated human-level spatial resolution and dynamic imaging capabilities under free-moving conditions. The system’s lightweight, compact design and wearable configuration offer new opportunities for brain PET imaging beyond the constraints of conventional static systems. The system now incorporates TOF reconstruction (timing resolution ~234 ps) and an optimized pile-up handling pipeline; remaining limitations are primarily lower sensitivity relative to whole-body PET/CT due to thinner crystals and limited detector coverage. Ongoing hardware (e.g., extended axial coverage) and software refinements (enhanced attenuation modeling and advanced/AI-assisted reconstruction) are expected to further improve image quality and quantitative accuracy. With continued improvements, SmartBrain has strong potential to support advanced neuroscience research and expand clinical applications in neurodegenerative diseases, movement disorders, and cognitive studies in naturalistic environments.

DISCLOSURE

This work was supported by the National Natural Science Foundation of China (Grant no. 82327809), National Key Research and Development Program of China (Grant No. 2024YFF0727400, 2024YFF0507700). This work was supported by Shenzhen Bay Laboratory High Performance Computing and Informatics Core. No potential conflicts of interest relevant to this article was reported. This study was approved by the Medical Ethics Committee of the Seventh Affiliated Hospital of Sun Yat-sen University (Approval No. KY-2024-354-02). All patients provided written informed consent prior to participation.

KEY POINTS

QUESTION: What is the performance of the SmartBrain PET, according to the NEMA NU 2-2018 standard?

PERTINENT FINDINGS: The SmartBrain PET provides a spatial resolution below 1.7 mm, a sensitivity of 720.15 cps/MBq, and a timing resolution of 234.22 ps.

IMPLICATIONS FOR PATIENT CARE: The SmartBrain PET system enables ambulatory imaging with enhanced cost-efficiency and a space-saving design, positioning it as a scalable solution for precision diagnostics in both clinical and community healthcare settings.

REFERENCES

1. Miyazaki T, Nakajima W, Hatano M et al. Visualization of AMPA receptors in living human brain with positron emission tomography. Nat Med. 2020;26:281–288.
2. Van Dyck CH, Swanson CJ, Aisen P, et al. Lecanemab in early Alzheimer's disease. N Engl J Med. 2023;388:9–21.
3. Yamamoto S, Honda M, Oohashi T, et al. Development of a brain PET system, PET-Hat: a wearable PET system for brain research. IEEE Trans Nucl Sci. 2011;58:668–673.
4. Tashima H, Yoshida E, Nishikido F, et al. Development of the helmet-chin PET prototype. IEEE Nucl Sci Symp Med Imaging Conf (NSS/MIC). 2015:1–3.
5. Melroy S, Bauer C, McHugh M, et al. Development and design of next-generation head-mounted ambulatory microdose positron-emission tomography (AM-PET) system. Sensors (Basel). 2017;17:1164.
6. Xu J, Zhao Z, Xie S, et al. Mind-tracker PET: a wearable PET camera for brain imaging. IEEE Nucl Sci Symp Med Imaging Conf (NSS/MIC). 2017:1–2.
7. Majewski S. The path to the "ideal" brain PET imager: the race is on, the role for TOF PET. Nuovo Cimento C. 2020;43:1–35.
8. Yu X, Liu H, Zhao H, et al. A multiplexing method based on multidimensional readout method. Phys Med Biol. 2025;70(4)
9. Tao W, Weng F, Chen G, et al. Design study of fully wearable high-performance brain PETs for neuroimaging in free movement. Phys Med Biol. 2020;65:135006.
10. National Electrical Manufacturers Association. NEMA Standards Publication NU 2-2018: performance measurements of positron emission tomographs. Rosslyn, VA: Natl Electr Manuf Assoc; 2018.
11. Zeng T, Yang H, Cao T, et al. Timing calibration comparison research of integrated TOF PET/MR. Sheng Wu Yi Xue Gong Cheng Xue Za Zhi. 2019;36:1003–1011.
12. Gong K, Cherry SR, Qi J. On the assessment of spatial resolution of PET systems with iterative image reconstruction. Phys Med Biol. 2020;65:225001
13. Pan T, Einstein SA, Kappadath SC, et al. Performance evaluation of the 5 - Ring GE Discovery MI PET/CT system using the National Electrical Manufacturers Association NU 2 - 2012 Standard. Med Phys. 2019;46:3025–3033.
14. Surti S, Karp JS. Update on latest advances in time-of-flight PET. Phys Med. 2020;80:251–258.
15. Gonzalez-Montoro, A., Pavón, N., Barberá, J. et al. Design and proof of concept of a double-panel TOF-PET system. EJNMMI Phys 11, 73 (2024).

16. Catana C. Development of dedicated brain PET imaging devices: recent advances and future perspectives. J Nucl Med. 2019;60:1044–1052.

17. Moliner L, Rodríguez-Alvarez MJ, Catret JV, et al. NEMA performance evaluation of CareMiBrain dedicated brain PET and comparison with the whole-body and dedicated brain PET systems. Sci Rep. 2019;9:15484.

18. Bartlett EA, Lesanpezeshki M, Anishchenko S, et al. Dynamic Human Brain Imaging with a Portable PET Camera: Comparison to a Standard Scanner. J Nucl Med. 2024;65(2):320-326.

19. Zhou F, D'Ascenzo N, Zhang B, et al. Development and evaluation of a portable MVT-based all-digital helmet PET scanner. IEEE Trans Radiat Plasma Med Sci. 2024;8:287–294.

20. Akamatsu G, Takahashi M, Tashima H, et al. Performance evaluation of VRAIN: a brain-dedicated PET with a hemispherical detector arrangement. Phys Med Biol. 2022;67:225011.

21. Li H, Badawi RD, Cherry SR, et al. Performance characteristics of the NeuroEXPLORER, a next-generation human brain PET/CT imager. J Nucl Med. 2024;65:1320–1326.

22. Siva NK, Bauer C, Glover C, et al. Real-time motion-enabling positron emission tomography of the brain of upright ambulatory humans. Commun Med. 2024;4:117.

23. Hu R, Li C, Tian K, Cui J, Chen Y, Liu H. Deep unrolled primal dual network for TOF-PET list-mode image reconstruction. Phys Med Biol. 2025;70(17).

24. Schramm G, Holler M. Fast and memory-efficient reconstruction of sparse Poisson data in listmode with non-smooth priors with application to time-of-flight PET. Phys Med Biol. 2022;67(15).

25. Murat H, Zulkifli MAA, Said MA, Awang Kechik M, Tahir D, Abdul Karim MK. Optimizing time-of-flight of PET/CT image quality via penalty β value in Bayesian penalized likelihood reconstruction algorithm. Radiography (Lond). 2025;31(1):343-349.

TABLE 1. INTRINSIC SPATIAL RESOLUTION MEASUREMENT

No	Z	X Offset (cm)	Average	Radial	Tangential	Axial
1	1/2	0	2.29	2.50	2.77	1.61
2		1	2.49	2.84	3.02	1.61
3		2	2.44	2.58	3.12	1.61
4		3	2.72	2.83	3.71	1.61
5		4	2.65	2.06	4.27	1.61
6		5	2.93	2.74	4.46	1.61
7		6	3.41	2.34	6.29	1.61
8		7	3.52	1.95	7.00	1.61
9	1/8	0	2.87	3.25	2.27	3.08
10		1	3.24	3.53	3.13	3.06
11		2	3.04	2.89	3.16	3.06
12		3	3.09	3.01	3.20	3.05
13		4	3.21	3.00	3.61	3.03
14		5	3.18	2.93	3.60	3.01
15		6	3.44	2.83	4.52	2.97
16		7	3.48	2.70	4.69	3.05

TABLE 2. CONTRAST RECOVERY COEFFICIENT AND BACKGROUND VARIABILITY FOR 12 ITERATIONS WITH 4 SUBSETS OF OSEM RECONSTRUCTION

Items	Sphere diameter j mm	Value
QH,j	10 mm	72.85%
	13 mm	76.88%
	17 mm	81.73%
	22 mm	80.40%
	28 mm	80.26%
	37 mm	89.40%
Nj	10 mm	11.25%

Genome-Wide Dual-Selection Unveils Novel Self-Cleaving Ribozymes in the Human Genome

Zhe Zhang[1], Jian Zhan[1,2,3*] and Yaoqi Zhou[1*]

[1]Institute for Systems and Physical Biology, Shenzhen Bay Laboratory, Shenzhen 518107, China
[2]Ribopeutic (Shenzhen) Co., Ltd., Futian, Shenzhen, Guangdong Province, 518000, China
[3]Ribopeutic Inc., Qiantang, Hangzhou, Zhejiang Province, 310018, China
[*] Co-corresponding authors (zhanjian@szbl.ac.cn and zhouyq@szbl.ac.cn)

Abstract

The landscape of catalytic RNA in complex eukaryotes remains poorly charted. Although self-cleaving ribozymes are widespread in microbial and viral genomes, their existence and functional roles in humans remain limited. Here, we introduce a generalizable, genome-wide discovery platform that integrates high-throughput signals from two complementary adapter ligation assays—3P-seq and 5OH-seq—to specifically capture RNA fragments bearing cleavage signatures (2′,3′-cyclic phosphate/3′-phosphate and 5′-hydroxyl termini). By applying a dedicated computational scoring algorithm to human genomic data, we systematically identified four previously unrecognized self-cleaving ribozymes. These ribozymes localize to diverse genomic features: an exon of WDFY1, an intron of PLD5 embedded within a repetitive element, an LTR retrotransposon, and the antisense strand of an SYNJ2BP intron. Truncation analyses defined minimal functional cores of ~70–100 nucleotides, and computational modeling suggests that they adopt novel structural architectures. Our work establishes a powerful strategy for transcriptome-wide mining of catalytic RNA, expands the catalogue of human ribozymes from 6 to 10, and reveals new layers of functional complexity in the human RNA world.

Main

Self-cleaving Ribozymes are an important class of non-coding RNAs with catalytic functions[1] that catalyze the site-specific self-cleavage of phosphodiester backbone[2]. Recent advancements in computational and high-throughput techniques have significantly accelerated the pace of ribozyme discovery[3,4]. However, the vast majority of self-cleaving ribozymes identified to date originate from lower organisms. Only 6 self-cleavage ribozymes are found in human so far (hammerhead ribozymes (HH9, HH10) located with introns[5], the HDV-like cytoplasmic polyadenylation element-binding protein 3 (CPEB3) ribozyme[6], 2 twister sister-like (TS-like) ribozymes[7] (LINE-1 and OR4K15), and the hovlinc ribozyme found in very long intergenic non-coding RNAs (vlincRNAs)[8]. Although these self-cleaving ribozymes lack structural similarity, they all accomplish site-specific cleavage through a nucleophilic attack by a 2′-oxygen on the adjacent phosphodiester bond. This reaction produces cleavage termini characterized by a 2′,3′-cyclic phosphate group and a 5′-hydroxyl group, respectively.

Previously, the Kapranov group utilized the RppH 5′ pyrophosphohydrolase and the XRN-1 5′-3′ exoribonuclease to degrade the other transcriptional products, except for the RNA fragments containing the 5′-hydroxyl. This led to the discovery of the hovlinc ribozyme among 28 candidates. Although the low discovery rate of self-cleaving ribozymes suggests the rarity in complex organisms, the question of whether other self-cleaving ribozymes exist in the human genome merits further study.

To probe the genome for potential self-cleaving ribozymes, we developed a strategy that leverages the unique specificity of RtcB ligase, an enzyme that joins a 5′-hydroxyl terminus to a 3′-phosphate or 2′,3′-cyclic phosphate terminus [9]. This was achieved by utilizing RtcB ligase in conjunction with specifically designed adapter RNAs to capture RNA molecules bearing these characteristic ends generated from self-cleavage. Among 96 candidate sequences subjected to experimental verification, six were confirmed to exhibit self-cleaving activity. Two of these active sequences had been documented previously, whereas the other four represent novel self-cleaving ribozymes. It is noteworthy that one self-cleaving ribozyme was identified within an exonic region of the WDFY1 (WD repeat and FYVE domain containing 1) protein, suggesting that it may play a direct role in regulating protein expression. To the best of our knowledge, this is the first report of a self-cleaving ribozyme residing in a protein-coding exon, and thus, significantly expands our understanding of the functional repertoire and mechanistic diversity of self-cleaving ribozymes.

Results

Genome-wide discovery of self-cleaving ribozymes

Genomic libraries were prepared using the Illumina tagmentation kit, which employs a Tn5 transposase to simultaneously fragment and tagmate DNA, streamlining the library construction process. Briefly, the tagmentation reaction fragmented genomic DNA and ligated Nextera s7 and Nextera s5 adapter sequences to both ends of the fragments in a single step. Then, the termini of the genomic library fragments were appended with T7 promoter through PCR amplification, facilitating downstream in vitro transcription (Fig. 1a). These RNA transcripts along with self-cleavage products obtained from the genomic library offers the distinct advantage of being unaffected by intracellular proteases. Unlike prior methods[8] that solely enriched for 5′-hydroxyl ends from self-cleavage, our approach specifically captures cleavage products containing either 2′,3′-cyclic phosphate or 5′-hydroxyl termini from self-cleavage. The 3P-seq is designed to isolate RNA fragments possessing 2′,3′-cyclic phosphate or 3′-phosphate ends. These 3′-ends were joined with a synthetic RNA linker that features a 5′-hydroxyl group by taking advantage of the unique ligation activity of RtcB ligase. Meanwhile, the 5OH-seq captures RNAs with 5′-hydroxyl termini by employing RtcB ligates these 5′-hydroxyl ends to a separate RNA linker that itself carries a 3′-phosphate group. A desthiobiotin modification was strategically engineered at the distal ends of both RNA linkers with a dual purpose: first, to minimize the formation of off-target ligation products, and second, to enable highly specific capture and enrichment by using streptavidin-based purification methods. The enriched products were subsequently processed into sequencing libraries for high-throughput analysis.

To minimize false positives, we employed paired-end sequencing and implemented a stringent quality filter based on the Mapping Quality (MAPQ) score from the SAM files, retaining only alignments with a MAPQ $\geqslant$ 30, which is widely regarded as a threshold for high-confidence mappings. The precise cleavage sites were inferred from the alignment boundaries, corresponding to the junctions between the inserted fragments and the adapter sequences. The distribution of these putative cleavage sites was then quantified by counting the supporting reads. During data processing, we observed that a substantial number of cleavage sites remained clustered within specific genomic regions. Given that self-cleaving ribozymes typically catalyze hydrolysis at unique sites, we rationalized that sites supported by an exceptionally low number of reads within these clusters were likely artifacts, potentially resulting from random RNA degradation. Consequently, a sophisticated denoising step was employed, which eliminated sites based on an intra-window signal intensity ratio. Furthermore, to enhance the reliability of our findings, we integrated the results from two independent experiments—3P-seq and 5OH-seq. A composite scoring system was designed to prioritize cleavage sites detected in both assays, under the premise that such "consensus" sites exhibit a lower probability of being false positives.

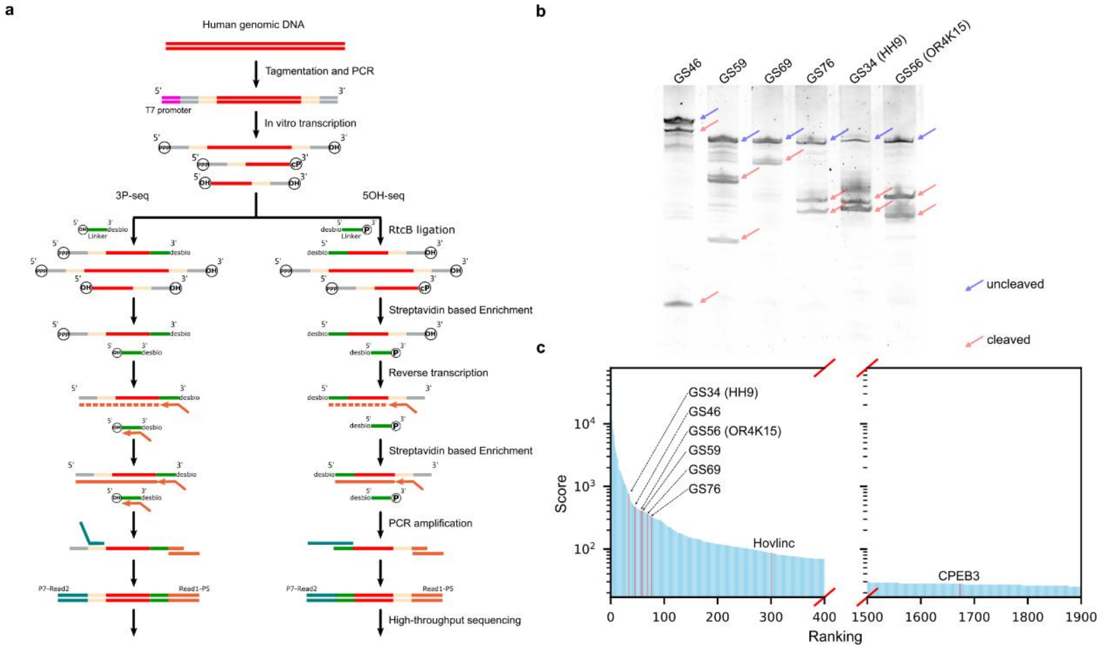

Fig. 1: Genome-scale discovery of self-cleaving ribozymes in human genome. a, The discovery flowchart: To profile RNA cleavage products, we generated a protease-resistant genomic RNA library through in vitro transcription. RtcB ligase and terminally modified RNA linkers were utilized to selectively capture and distinguish fragments bearing 2′,3′-cyclic phosphate or 5′-OH ends, followed by streptavidin bead enrichment and sequencing library construction. b, Urea PAGE analysis of the six experimentally validated ribozyme candidates from the top 96 hits. Hit nomenclature reflects its ranking (e.g., GS46 corresponds to the hit ranked 46th). c, Scoring distribution of the top 1,900 hits. Hits corresponding to known ribozymes and novel ribozymes that have been validated through experiments are explicitly marked in red.

Self-cleaving ribozymes identified in HeLa genome

Applying this integrated approach, we successfully identified four out of the five known self-cleaving ribozymes, with HH9 and OR4K15 ranking within the top 96 hits (Fig. 1b). However, the hovlinc ribozyme, discovered more recently, was ranked 301st (Fig. 1c), primarily due to its low detection count (2 reads) in the 5OH-seq assay. The CPEB3 ribozyme was ranked 1,673rd (Fig. 1c) and was not detected in the 5′OH-seq assay.

To gain some understanding of low priority in hovlinc and CPEB3 ribozymes, we generated normalized coverage files from the BAM files and visualized the signal intensity across the targeted gene regions by using the deepTools suite[10]. Analysis of the signal profiles across identified ribozymes shows a spectrum: from those with a pronounced signal asymmetry (Fig. 2a, 2c, 2f, 2g and 2h) to those with relatively balanced signals at both ends (Fig. 2b, 2d and 2e). This variation is principally dictated by the unique sequence and the consequent secondary/tertiary structure of each ribozyme, which directly affects the mapping efficacy of the RNA linkers during the library preparation. These inherent structural differences are a major source of the significant variation in observed sequencing depth. For hovlinc and CPEB3 ribozymes, their characteristically stable 3′ terminal structures likely impede efficient adapter ligation, resulting in negligible 3′ end capture signal and thus a substantially lower ranking in our analysis, highlighting a specific limitation in detecting self-cleaving ribozymes with such structural features.

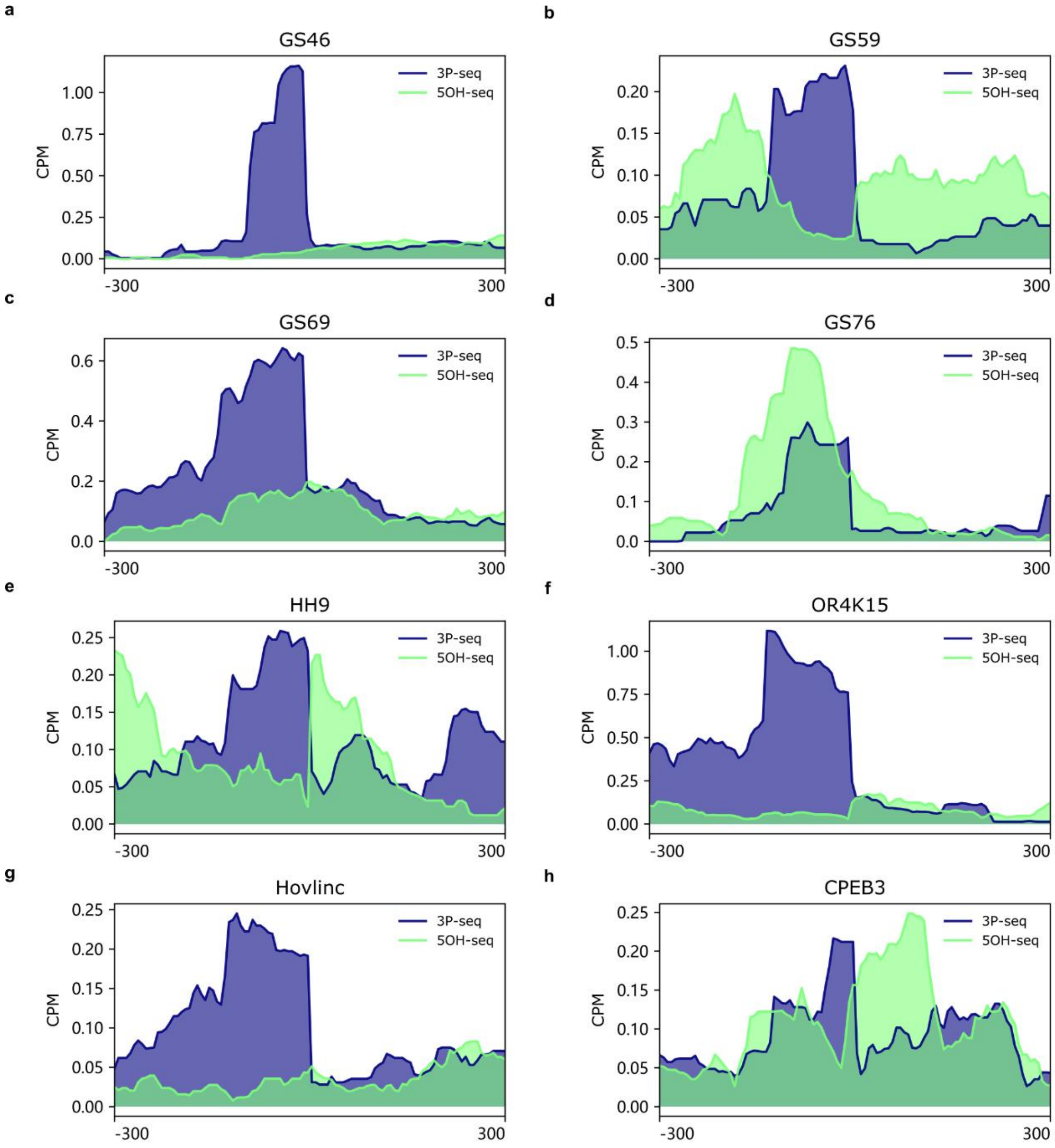

Fig. 2: Normalized signal from the two genome-wide selection assays. The y-axis represents the counts per million (CPM) of mapped reads, while the x-axis corresponds to a 600-nucleotide (nt) genomic window centered on the cleavage site. a–d illustrate four novel ribozymes identified in this study. e and f depict two previously reported ribozymes (HH9 ranked 34th, OR4K15 ranked 56th) that were confirmed among the top 96 validated sequences in our screening. In contrast, g and h show two known ribozymes that ranked lower in our results, indicating their relatively lower abundance or activity under the experimental conditions.

New ribozymes with potential novel function

We characterized four novel self-cleaving ribozymes (GS46, GS59, GS69, GS76), each occupying a distinct genomic locus that suggests unique regulatory potentials. Particularly notable is GS46, which was located within the eighth exon of the protein-coding gene WDFY1 (WD repeat and FYVE domain containing 1); its self-cleavage activity is thus supposed to truncate the host mRNA, potentially triggering nonsense-mediated decay and leading to reduced expression of the WDFY1 protein. Furthermore, GS59 and GS69 were identified within repetitive genomic architectures: GS59 was situated in the first intron of PLD5 (Phospholipase D Family Member 5) and embedded within a DNA repeat element, while GS69 was found within an intron of a novel transcript that itself resides in a Long Terminal Repeat (LTR) retrotransposon. Additionally, GS76 was mapped to the reverse (antisense) strand of the first intron of the SYNJ2BP (Synaptojanin 2 Binding Protein) gene, an intriguing location that raises the possibility of its involvement in regulating the sense transcript.

To elucidate the structural basis of the self-cleaving activity, we conducted a preliminary investigation of the four newly identified ribozymes. It is important to note that the RNA fragments captured in our sequencing libraries do not necessarily represent the minimal structural module required for catalytic activity as we demonstrated previously[7]. Therefore, to delineate the core functional domain of each ribozyme, we systematically generated a series of truncated variants. Given that the 3P-seq assay yielded stronger signals for most of these ribozymes (Fig. 2), indicating a more defined or stable 3′ end post-cleavage, the truncation strategy primarily involved progressive shortening from the 3′ terminus. The catalytic competence of these truncated constructs was then assessed by analyzing their self-cleavage efficiency via polyacrylamide gel electrophoresis (PAGE). This empirical approach allowed us to identify the minimal functional core for each ribozyme, with optimized lengths of approximately 70 nt, 100 nt, 80 nt, and 80 nt, respectively (Fig. 3a). Subsequent computational prediction of the secondary and tertiary structures for these minimized variants suggested that each adopts a distinct and previously uncharacterized structural fold (Fig. 3b), potentially representing novel architectural classes among self-cleaving ribozymes.

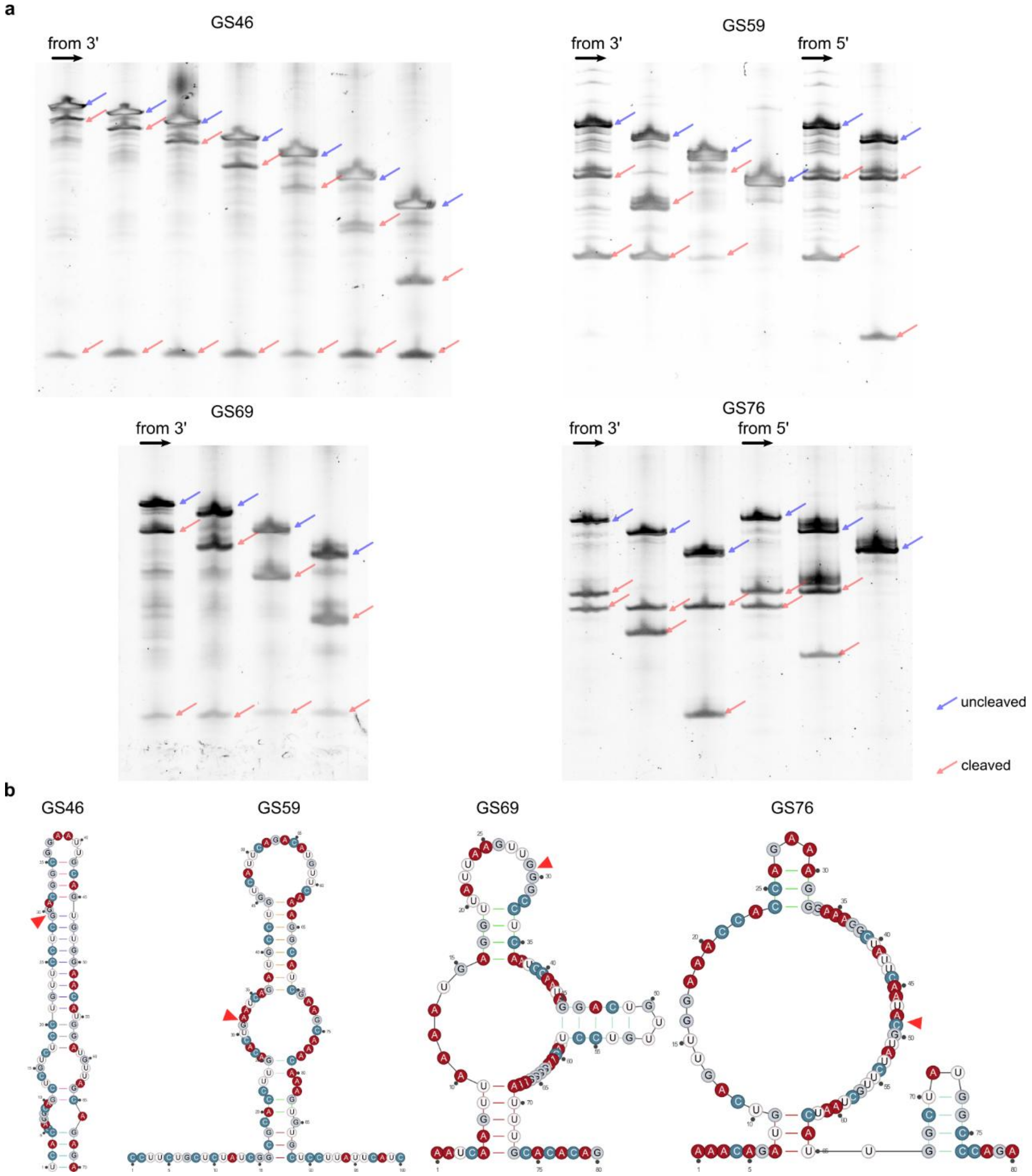

Fig. 3: Truncations and predicted secondary structures of the 4 new ribozymes. a, PAGE analysis of the truncated variants of the 4 new ribozymes. A series of truncated variants was generated from the original sequence for activity assay. The 3′ end (or 5′ end) was anchored, and sequential 20-nt

deletions were made from the opposite terminus. This process continued until the whole fragment reached a minimum length of 100 nt, which was determined to be optimal for efficient molecular cloning. b, Predicted secondary structure of the minimal truncated ribozymes. The secondary structures of the RNA sequences were predicted by employing the computational tool SPOT-RNA[11]. The red triangle indicates the cleavage site.

Discussion

Self-cleaving ribozymes are ubiquitous in lower organisms, yet their representation in complex eukaryotic genomes remains enigmatic. Although prior studies have identified a handful of examples in humans—including the HDV-like CPEB3 ribozyme[6], two hammerhead ribozymes[5], and the hovlinc ribozyme[8]—these discoveries relied heavily on known sequence motifs，specific biochemical properties or genome-scale search according to the discovery of hovlinc ribozyme[8]. This raises a fundamental question: is the scarcity of known human ribozymes biological reality, or a reflection of methodological constraints?

To address this, we developed a high-throughput, unbiased discovery pipeline centered on a defining catalytic product: RNA fragments with 2′,3′-cyclic phosphate and 5′-hydroxyl termini. Our key innovation is the dual-selection of both termini using RtcB ligase, which concurrently requires both cleavage signatures. This strategy dramatically enhances specificity over single-end capture methods and provides a generalizable framework for transcriptome-wide ribozyme mining.

Applying this approach, we discovered four novel self-cleaving ribozymes from the human genome. Notably, their genomic contexts suggest diverse functional and evolutionary origins. Ribozyme GS46 resides in a protein-coding exon of WDFY1, implying a potential role in post-transcriptional regulation, possibly through cleavage-mediated nonsense-mediated decay of its host mRNA. In contrast, GS59 and GS69 are embedded within repetitive elements—an intronic DNA repeat in PLD5 and an LTR retrotransposon, respectively—hinting at mobilization via genomic dynamics. The antisense localization of GS76 within an SYNJ2BP intron suggests possible cis-regulation of the sense transcript through mechanisms like RNA interference. Truncation analyses defined minimal functional cores (~70–100 nt), and computational modeling indicates these adopt novel structural folds, pointing to potentially new ribozyme classes.

Our method represents a significant advance in discovery efficiency. From 96 high-confidence candidates, we validated six active sequences—including two known and four novel ribozymes—substantially outperforming previous motif-, similarity-based and biochemical enrichment-based searches. However, the presence of false positives underscores the necessity for rigorous experimental validation. These signals may originate from trans-cleavage events, non-specific enzymatic reactions, or other RNA processing activities; their resolution will be crucial for future pipeline optimization.

A technical limitation of our RtcB-based capture is variable detection sensitivity across ribozyme classes, as evidenced by the weak signal for hovlinc and the absence of signal for CPEB3 in 5OH-seq data. Stable 3′-terminal secondary structures or post-ligation cleavage may impair adapter ligation efficiency, suggesting areas for methodological refinement.

In summary, this work significantly expands the catalog of human self-cleaving ribozymes and provides a powerful, adaptable strategy for their discovery. The unique genomic associations and putative novel structures of the identified ribozymes open new avenues for exploring RNA catalysis in eukaryotic regulation. Future efforts to determine their tertiary structures, precise mechanisms, and biological functions will deepen our understanding of the functional complexity of the human RNA world.

Methods

Experimental process for ribozyme identification

HeLa genomic DNA libraries were constructed using the tagmentation method, which simultaneously fragments genomic DNA (NEB, no. N4006S) and incorporates adapter sequences via the Tn5 transposase. The process was performed using the Nextera XT DNA Library Preparation Kit (Illumina), following the manufacturer′s guidelines. PCR amplification of the tagmentation product was carried out using primers T7p-s7 and T7t-s5. These primers were designed to anneal to the Nextera s7 and s5 adapter regions, respectively, and incorporated the T7 promoter sequence at the 5′ ends of the amplicons. Separation of the DNA library fragments (500-1000 bp) was achieved by agarose gel electrophoresis and subsequent gel purification.

Purified DNA library was then used as the template for in vitro transcription by incubation with 100 U of T7 RNA Polymerase (NEB, no. M0251L) in 1×T7 RNA polymerase buffer (40 mM Tris-HCl pH 7.9, 6 mM $MgCl_2$, 1 mM DTT, 2 mM spermidine) with 2 mM NTP mix (NEB, no. N0466S) and 20 U Murine RNase Inhibitor (NEB, no. M0314S) in a 30 µl reaction volume for 5 h at 37 °C. DNA templates were removed by incubation with 2 U of DNase I (NEB, no. M0303S) and 1× DNase I reaction buffer in a 100 µl volume at 37 °C for 15 min, followed by purification with RNA Clean & Concentrator-5 kit (Zymo Research, no. R1016).

2.5 µg purified RNA were incubated with 100 pmol linker (rM13F_3desBio for 3P-seq, rM13R_5desBio_3P for 5OH-seq) in 1× RtcB reaction buffer with 22.5 pmol RtcB ligase (NEB, no. M0458S), 0.1 mM GTP and 1 mM $MnCl_2$ in 30 µl at 37 °C for 1 h. Ligation products were purified with Sera-Mag Streptavidin-Coated Magnetic Beads (Cytiva, no. 30152103010150) and eluted in 20 µl TNB buffer (20 mM Tris-HCl pH 7.5, 150 mM NaCl, 4 mM biotin). Before reverse transcription, ligation products were exchanged into H_2O by column purification.

Ligation products were reversed transcribed using primer (RT1_m13f_adp1 for 3P-seq, RT1_Tn5ME_adp1 for 5OH-seq) and the ProtoScript II Reverse Transcriptase (NEB, no. M0368S). Ligation product was first denatured at 65 °C for 5 min in a 19.5 µl volume containing 1 µl of 100 µM primer and 1.5 µl of 10 mM dNTP mix, followed by rapid snap-cooling on ice for 2 min. Then, 6 µl of 5 × ProtoScript II Reverse Transcriptase buffer, 3 µl of 0.1 M DTT, 0.5 µl of Murine RNase Inhibitor (NEB, no. M0314S) and 1 µl of ProtoScript II Reverse Transcriptase were added and incubated at 42 °C for 1 h and then 65 °C for 20 minutes to inactivate the enzyme, followed by enrichment with Sera-Mag Streptavidin-Coated Magnetic Beads (Cytiva, no. 30152103010150) and clean-up by using RNA Clean & Concentrator-5 kit (Zymo Research, no. R1016).

Purified cDNA was amplified by touch-up PCR using primers (P7R2_Tn5ME/P5R1_adp1 for 3P-seq, P7R2_m13r/P5R1_adp1 for 5OH-seq) with Q5 Hot Start High-Fidelity DNA Polymerase (NEB, no. M0493S) to construct the high-throughput sequencing library. The PCR products were purified with homemade magnetic beads mix, and sequenced on an Illumina HiSeq X sequencer with 20% PhiX control by Novogene Technology Co., Ltd.

High-throughput sequencing data analysis

A standard bioinformatic pipeline was implemented to process the sequencing data. Briefly, adapter sequences were trimmed from the raw reads using Cutadapt[12]. To ensure stringent removal of the short adapter sequences flanking our library constructs, the Cutadapt-processed reads were further filtered with a custom script. This step involved removing the last 5 nucleotides from all reads longer than 113 nt. The resulting high-quality paired-end reads were then aligned to the UCSC human reference genome (hg38) using Bowtie2[13] in the --very-sensitive mode. The subsequent SAM file was processed to retain only uniquely mapped, properly paired reads with a MAPQ score of 30 or higher. Finally, the alignment data for each read was converted into cleavage site information, and all potential sites were statistically tallied and ranked.

Cleavage sites that appeared only once were filtered out, retaining only those sites with a read count of at least two. Noise reduction was then performed using a custom script. This method functions by analyzing the signal intensity ratios within sequencing reads of a defined window size. All potential cleavage sites within a defined genomic window (50nt) are removed if more than one site is present and the signal intensity ratio between them is less than 10. Each potential cleavage site was subsequently assigned a score calculated as (N_5OH + 1) × (N_3P + 1), where N_5OH and N_3P represent the number of occurrences of the site in the 3P-seq sequencing library and the 5OH-seq sequencing library, respectively. The top 96 ranked sequences by score, were selected as the final candidate pool for experimental validation.

Experimental validation of candidate sequences

The top 96 candidate sequences, each flanked with the T7 promoter and unique index sequences, were synthesized as an oligo pool by IDT (Integrated DNA Technologies). The oligo pool was subsequently PCR-amplified with specific forward and reverse primers to obtain the target genes. PCR products were cloned into the pUC57 vector through homologous ends encoding the T7 promoter and a NotI site by using the HiFi DNA Assembly Master Mix (NEB, no. E2621L). After chemical transformation, single colonies containing the candidate sequences were picked for downstream validation. The candidate DNA templates were transcribed in vitro for 5 hours using T7 RNA Polymerase (NEB, no. M0251L). The transcription products were digested with DNase I (NEB, no. M0303S) and denatured at 70°C for 5 min after adding an equal volume of 2 × RNA Loading Dye (NEB, no. B0363S) for subsequent denaturing PAGE analysis.

Experimental validation of ribozyme variants

All truncated variants were generated via in vitro recombination using a Seamless Cloning kit (Beyotime, no. D7010M). Specifically, each variant was amplified with a pair of primers containing homologous arms flanking the T7 promoter and a NotI restriction site, and then cloned into the pUC57 vector through homologous recombination. Variants containing SNPs were constructed by site-directed mutagenesis using primers encoding the desired point mutations. The entire plasmid was amplified with these mutagenic primers, and the parental DNA template was digested with DpnI (NEB, no. R0176S). The digested product was subsequently transformed into E. coli DH5α cells. All constructed variants were verified by Sanger sequencing. Plasmid DNA from sequence-verified clones was linearized by NotI (NEB, no. R3189S) digestion and served as the template for in vitro transcription. Transcription reactions were performed using the T7 RNA Polymerase (Beyotime, no. R7012L), following the manufacturer's protocol. After transcription, the DNA template was removed by DNase I (NEB, no. M0303S) treatment. The RNA products were then incubated in 1× TKMS buffer (50 mM Tris-HCl pH 8.0, 25mM KCl, 10 mM $MgCl_2$, 2 mM spermidine) at 37°C for 2 hours. Finally, the RNA was purified and analyzed by 10% denaturing polyacrylamide gel electrophoresis (PAGE), followed by staining with SYBR Gold nucleic acid gel stain (Thermo Fisher, no. S11494).

Reference

1. Cech, T. R. Evolution of biological catalysis: ribozyme to RNP enzyme. *Cold Spring Harb Symp Quant Biol* **74**, 11–16 (2009).
2. Jimenez, R. M., Polanco, J. A. & Lupták, A. Chemistry and biology of self-cleaving ribozymes. *Trends Biochem Sci* **40**, 648–661 (2015).
3. Roth, A. *et al.* A widespread self-cleaving ribozyme class is revealed by bioinformatics. *Nat Chem Biol* **10**, 56–60 (2014).
4. Weinberg, Z. *et al.* New classes of self-cleaving ribozymes revealed by comparative genomics analysis. *Nat. Chem. Biol.* **11**, 606–610 (2015).
5. de la Peña, M. & García-Robles, I. Intronic hammerhead ribozymes are ultraconserved in the human genome. *EMBO Rep.* **11**, 711–716 (2010).

6. Salehi-Ashtiani, K., Lupták, A., Litovchick, A. & Szostak, J. W. A genomewide search for ribozymes reveals an HDV-like sequence in the human CPEB3 gene. *Science* **313**, 1788–1792 (2006).
7. Zhang, Z. *et al.* Minimal twister sister-like self-cleaving ribozymes in the human genome revealed by deep mutational scanning. *Elife* **12**, RP90254 (2024).
8. Chen, Y. *et al.* Hovlinc is a recently evolved class of ribozyme found in human lncRNA. *Nat Chem Biol* https://doi.org/10.1038/s41589-021-00763-0 (2021) doi:10.1038/s41589-021-00763-0.
9. Tanaka, N., Chakravarty, A. K., Maughan, B. & Shuman, S. Novel mechanism of RNA repair by RtcB via sequential 2',3'-cyclic phosphodiesterase and 3'-Phosphate/5'-hydroxyl ligation reactions. *J. Biol. Chem.* **286**, 43134–43143 (2011).
10. Ramírez, F. *et al.* deepTools2: a next generation web server for deep-sequencing data analysis. *Nucleic Acids Res* **44**, W160-165 (2016).
11. Singh, J., Hanson, J., Paliwal, K. & Zhou, Y. RNA secondary structure prediction using an ensemble of two-dimensional deep neural networks and transfer learning. *Nat Commun* **10**, 5407 (2019).
12. Martin, M. Cutadapt removes adapter sequences from high-throughput sequencing reads. *EMBnet.journal* **17**, 10–12 (2011).
13. Langmead, B. & Salzberg, S. L. Fast gapped-read alignment with Bowtie 2. *Nature Methods* **9**, 357–359 (2012).